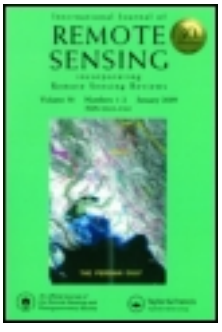

International Journal of Remote Sensing

Publication details, including instructions for authors and subscription information:
http://www.tandfonline.com/loi/tres20

Achieving downscaling of Meteosat thermal infrared imagery using artificial neural networks

Stavros Kolios [a], George Georgoulas [a] & Chrysostomos Stylios [a]

[a] Knowledge and Intelligent Computing Laboratory, Informatics and Telecommunication Technology, TEI of Epirus, 47100, Arta, Greece

Published online: 02 Sep 2013.

To cite this article: Stavros Kolios, George Georgoulas & Chrysostomos Stylios (2013) Achieving downscaling of Meteosat thermal infrared imagery using artificial neural networks, International Journal of Remote Sensing, 34:21, 7706-7722

To link to this article: http://dx.doi.org/10.1080/01431161.2013.825384

International Journal of Remote Sensing, 2013
Vol. 34, No. 21, 7706–7722, http://dx.doi.org/10.1080/01431161.2013.825384

Taylor & Francis
Taylor & Francis Group

Achieving downscaling of Meteosat thermal infrared imagery using artificial neural networks

Stavros Kolios*, George Georgoulas, and Chrysostomos Stylios

Knowledge and Intelligent Computing Laboratory, Informatics and Telecommunication Technology, TEI of Epirus, 47100 Arta, Greece

(*Received 23 July 2012; accepted 16 March 2013*)

This study presents the successful application of artificial neural networks (ANNs) for downscaling Meteosat Second Generation thermal infrared satellite imagery. The scope is to examine, propose, and develop an integrated methodology to improve the spatial resolution of Meteosat satellite images. The proposed approach may contribute to the development of a general methodology for monitoring and downscaling Earth's surface characteristics and cloud systems, where there is a clear need for contiguous, accurate, and high-spatial resolution data sets (e.g. improvement of climate model input data sets, early warning systems about extreme weather phenomena, monitoring of parameters such as solar radiation fluxes, land-surface temperature, etc.). Moderate Resolution Imaging Spectroradiometer (MODIS) images are used to validate the downscaled Meteosat images. In terms of the ANNs, a multilayer perceptron (MLP) is used and the results are shown to compare favourably against a linear regression approach.

1. Introduction

Since the early 1970s, geostationary satellites have been gathering huge amounts of data and providing useful information about the atmosphere. Nowadays, the modern geostationary satellite sensors (such as the spinning enhanced visible infrared imager (SEVIRI) instrument on board the Meteosat-9 satellite) are designed to provide useful data to the scientific community and information about the Earth's surface and atmosphere. More specifically, the Meteosat-9 satellite belongs to the category of Meteosat Second Generation (MSG) satellites launched by the European Space Agency (ESA) and currently constitutes the main meteorological satellite platform above Europe and Africa positioned at 0° latitude and longitude, and 36,000 km above Earth's surface. Parameters such as winds at different atmospheric levels, concentrations of major atmospheric components (e.g. carbon dioxide and ozone), cloud systems, precipitation, and many other phenomena and parameters can be detected, retrieved, and finally monitored using MSG data sets as initial information (Schmetz et al. 2002). The satellite data obtained from the SEVIRI instrument are provided operationally at a high temporal resolution (nominally 15 min, or 5 min in the rapid scan mode) and a varying spatial resolution of 3 km at the sub-satellite point (SSP), which decreases in mid-latitudes to approximately 4–5 km. The thermal infrared (TIR) imagery of the SEVIRI instrument provides data from eight different channels ranging from 3.9 to 13.4 μm (Schmetz et al. 2002). The TIR imagery plays a crucial role in detecting, monitoring,

*Corresponding author. Email: stavroskolios@yahoo.gr

and forecasting cloud evolution and a series of atmospheric characteristics (e.g. Kolios and Feidas 2012; Georgiev and Kozinarova 2009; Vila et al. 2008; Setvak et al. 2008; Stisen et al. 2007; Sun and Pinker 2007; Morel and Senesi 2002) through gathering contiguous data flow during both day and night. In this way, TIR data provide valuable information especially in monitoring parameters that vary significantly on a daily basis.

Nevertheless, for many applications, the retrieved parameters require data not only with high temporal but also high spatial resolution. In order to improve the spatial resolution of satellite images, many downscaling methodologies – i.e. the conversion of data from a coarser spatial resolution to a finer one (Stein et al. 1998) – are used. Indeed, there is a variety of such methodologies that are classified into different categories according to the kind and the quality of the initial data set and the initial–final spatial difference (Van der Meer 2012; Wilby et al. 2004).

Downscaling procedures are widely used to convert large-scale estimation of physical parameters (e.g. precipitation and temperature) produced by general circulation models into finer-scale data sets (Wilby 1998; Dibike and Coulibaly 2006; Hessami et al. 2008; Kioutsioukis, Melas, and Zanis 2008; Chu et al. 2010).

During the last decade, downscaling methodologies have been increasingly used also for remotely sensed data. International literature incorporates many studies (Van der Meer 2012) about downscaling moderate resolution remotely sensed data from polar-orbiting satellites to a finer resolution using a variety of different techniques. For example, in the study of Liu and Pu (2008), two different downscaling approaches were used to retrieve spatially improved land-surface temperature (LST) pixel values based on TIR imagery of the Moderate Resolution Imaging Spectroradiometer (MODIS) and Advanced Spaceborne Thermal Emission and Reflection (ASTER) sensors. Stathopoulou and Cartalis (2009) examined four different downscaling methodologies to improve the spatial resolution of the estimated LST from the TIR images of the Advanced Very High Resolution Radiometer (AVHRR). They achieved a downscaling at 120 m from the 1000 m that were the initial data. Zutita-Milla et al. (2009) used linear mixing model techniques in order to downscale Medium Resolution Imaging Spectrometer (MERIS) data from a moderate spatial resolution (about 1 km) to 30 m in order to study vegetation seasonal dynamics. Moreover, Zhang et al. (2012) used two well-known geostatistical methods (ordinary kriging and co-kriging) for downscaling spatial resolution of remotely sensed atmospheric methane column concentrations retrieved from the Scanning Imaging Absorption Spectrometer for Atmospheric Chartography (SCIAMACHY) instrument (on board the Envisat satellite platform).

Nevertheless, studies concerning the downscaling of data from geostationary satellites and especially for the MSG data remain sparse. Downscaling of Meteosat data can improve their initial spatial resolution and increase their usefulness. In a recent study, the radiances of the 0.6 and 0.8 μm visible MSG channels (3 km resolution at SSP) were downscaled to the moderate resolution of 1 km (Deneke and Roebeling 2010). The results of this study were promising in terms of the reflectance in the aforementioned channels. Zakšek and Schroedter-Homescheidt (2009) downscaled the LST product of MSG in order to calculate and monitor air temperature with significant accuracy. In another study, related to the downscaling of MSG data, Sandholt, Nielsen, and Stisen (2009) focused on the assessment of LST using spatially improved SEVIRI data sets. In a more recent study, Zakšek and Oštir (2012) downscaled LST SEVIRI data using moving window analysis in order to study urban heat island diurnal cycles. To sum up, there is significant merit in downscaling the initial operational Meteosat data set for operational purposes to derive additional parameters at a higher spatial resolution than the initial data.

The scope of this study is to apply and evaluate the use of artificial neural networks (ANNs) in order to improve the spatial resolution (downscale) of the operational SEVIRI data (High Rate Information Transmission (HRIT) data). These are widely used in the TIR spectral region (9.8–11.8 μm) to provide contiguous data flows during both day and night.

The rest of the article is structured as follows. Section 2 describes the involved data sets as well as the proposed downscaling methodology. Section 3 presents the implementation of the proposed downscaling technique for a representative data set and the results are compared with those of a linear downscaling model. Finally, Section 4 concludes the article by providing a discussion on the results, along with some ideas for future work.

2. Data and methodology

In this study, data from the SEVIRI instrument on board the Meteosat-9 geostationary satellite and data from MODIS on board the Terra/Aqua polar-orbiting satellites were collected and integrated. Regarding SEVIRI, channels 9 (9.8–11.8 μm) and 10 (11.0–13.0 μm) were used for downscaling the initial spatial resolution (3 km at the SSP and around 4–5 km at mid-latitudes) imagery of channel 9 to a finer resolution that reaches the spatial resolution of MODIS TIR scenes (1.1 km). The MODIS images in channel 31 (10.78–11.28 μm) were used as reference data. The Meteosat-9 and MODIS scenes were collected via the European Organization for the Exploitation of Meteorological Satellites (EUMETSAT) Data Centre and the Level 1 and Atmosphere Archive and Distribution System (LAADS) of NASA, respectively.

2.1. Preprocessing

Synoptically, regarding the preprocessing stage of the initial SEVIRI and MODIS data sets, the following steps are followed.

(1) All pixel values of all used image scenes and channels – of either SEVIRI or MODIS – are converted from digital numbers to brightness temperatures (BTs).
(2) All SEVIRI and MODIS images are georeferenced at the World Geodetic System 1984 (WGS-84) datum.
(3) A low-frequency 3 × 3 filter (gamma filter) is applied to MODIS data in order to suppress the existence of the observed striping in the used image scenes.

2.2. Data sample

As mentioned above, the aim of this study is to investigate the use of ANNs for estimating the BT values at a finer spatial resolution than the initial Meteosat geostationary satellite imagery. MODIS images were used as reference images because our intention was to downscale the TIR imagery of Meteosat, which provides data even at night.

It is known that successful implementation of ANNs requires the selection of a balanced and representative training data set. In an effort to select the training data set with the widest possible temperature range, two MODIS scenes at two different seasons of the year (summer and winter) were selected. It was decided to use data from two different seasons, aiming to collect pixel values (BTs) corresponding to different upwelling radiation values and different emissivity of the Earth's surface and atmosphere in the TIR. More precisely, the MODIS scenes were those acquired on 5 January 2010 (19:55 UTC) and

16 August 2010 (20:50 UTC). The corresponding SEVIRI images were also gathered at the same dates and times (19:45 and 20:45 UTC, but at HRIT data temporal resolution and naming convention). It must be noted that the actual difference between the scenes compared between MODIS and SEVIRI is less than the typical time difference apparent from MODIS and SEVIRI names of image files. This is due to the SEVIRI sensor scanning mode. More specifically, the scanning procedure lasts a little under 15 min, so the mid-latitudes of the northern hemisphere are scanned at about 10–12 min after the initiation of every new scan (Kolios 2009). Consequently, the actual time difference obtained from MODIS and SEVIRI images is about 5 min or even less. Figures 1 and 2 depict the MODIS subsets of the image scenes that are used to select the training sample as well as their corresponding SEVIRI image, which covers a greater area. It must be noted also that in the SEVIRI subsets of Figures 1 and 2, the time refers to the typical (not the actual) time of scanning the features shown.

In each MODIS image scene, a set of pixels was chosen in order to represent a wide range of thermally different features at satellite images for such a spatial resolution. For the chosen sets of pixels, their relative BTs in channel 31, as well as their geographical coordinates, are stored and spatially correlated with the SEVIRI imagery (Figure 3).

The spatial correlation of MODIS and SEVIRI pixel values (BTs) is an issue of crucial importance with respect to collecting a representative and accurate data set for ANN training. For this reason, except for the georeference of two different satellite data to the same system (WGS-84), an image-to-image registration was applied.

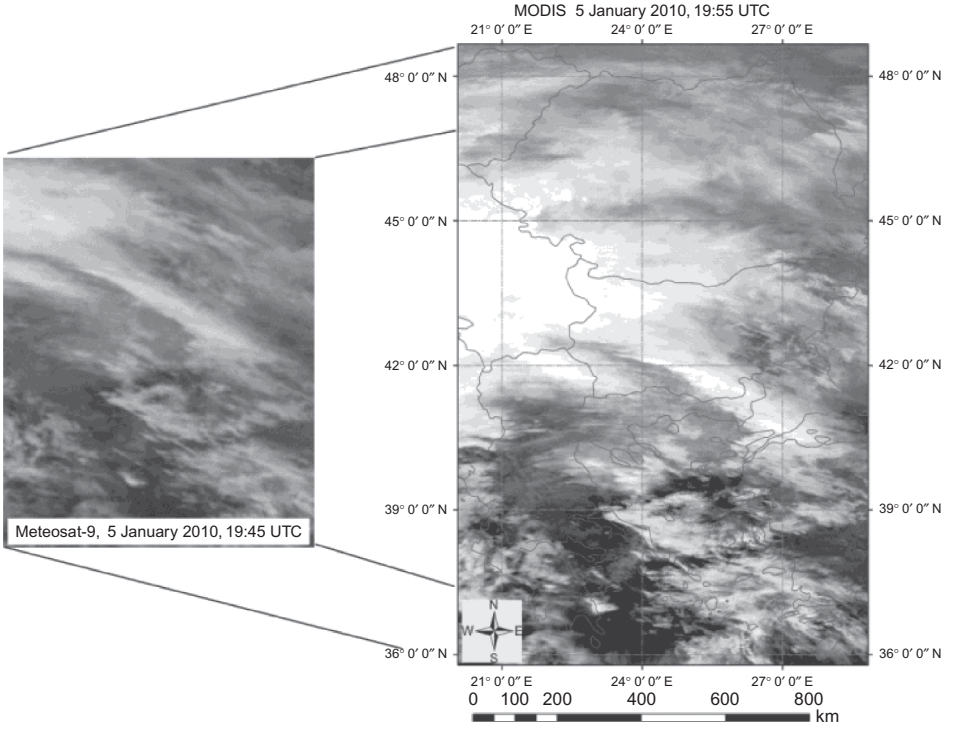

Figure 1. Subset of MODIS image scene on 5 January 2010, 19:55 UTC (10.78–11.28 μm channel), and its most closely related Meteosat-9 image (9.8–11.8 μm channel).

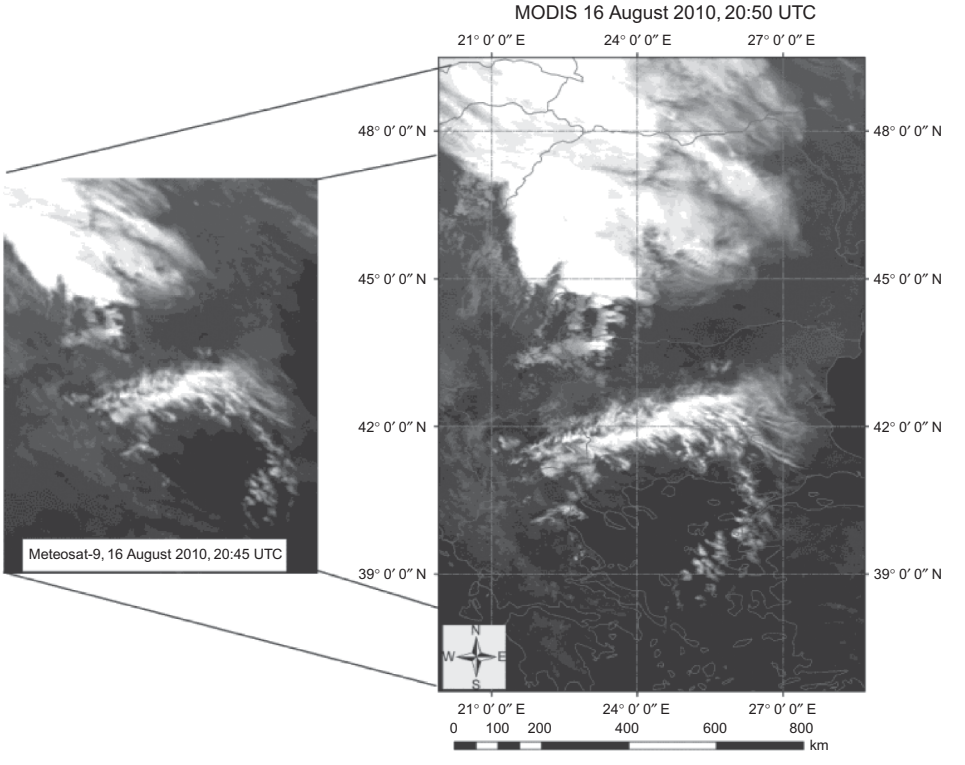

Figure 2. Subset of MODIS image scene on 16 August 2010, 20:50 UTC (10.78–11.28 μm channel), and its most closely related Meteosat-9 image (9.8–11.8 μm channel).

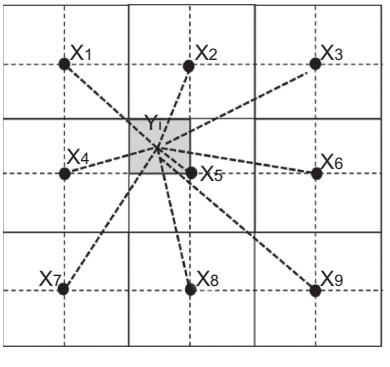

Figure 3. The nine Meteosat-9 pixels (X_j) are considered to be correlated with a given MODIS pixel (Y_i). The black solid lines represent Meteosat-9 pixels with their centres (black dots). The dotted lines represent the MODIS pixels in ideally correlated grids.

In this study, we did not use the classical and widely used approach for image-to-image registration based on ground control points (GCPs) and polynomial transformations. In practice, the use of a polynomial transformation and resampling method would result in a severe vitiation in the initial pixel values of the chosen images to be registered (SEVIRI images) to the other (MODIS images). Even if we used a large number of well-distributed

and carefully selected GCPs, the different nature of MODIS (instrument in polar-orbit) and SEVIRI (instrument in geostationary orbit) on the one hand, and the different field of views, scanning modes, and spatial resolution in the comparable TIR channels, on the other hand, would lead to significant deformation of the registered images. In addition to this, the coarse spatial resolution of SEVIRI TIR imagery and the small but not negligible time difference between the relative MODIS and SEVIRI scenes creates considerable difficulty in distinguishing specific features to be used as GCPs and consequently leads to an inaccurate spatial correlation between MODIS and SEVIRI pixels. Considering the above issues, the classical GCPs and polynomial transformations methodology for an image-to-image registration could lead to significant inaccuracies, especially for large geographical areas and for all possible features that could be extracted in such spatial resolutions.

Thus, an alternative image-to-image spatial correlation approach was followed. More analytically, for a given MODIS pixel, nine SEVIRI pixels with the smallest distances (great circle distances) from the specific MODIS pixel are selected and considered as the most relative SEVIRI pixels to a given MODIS pixel. Figure 3 presents a typical application of this spatial correlation. This procedure is automated and is implemented using a module written in the VB.NET programming language environment. Figure 3 illustrates how nine SEVIRI pixels (pixels with their respective dimensions and centres are depicted by black solid lines and black circles, respectively) can contribute to the estimation of a given MODIS pixel (grey pixel).

This image-to-image registration procedure was followed in order to eliminate georeferencing errors and in general all factors that could incorporate geometric errors during the spatial correlation of two different satellite data, changing at the same time as little as possible the initial pixels values of the SEVIRI images and consequently their BTs.

Following the above-mentioned approach, a total of 281,069 MODIS pixels were selected for the two reference image scenes. For these pixels, a module in the VB.NET programming language was developed as previously mentioned in order to implement the image-to-image registration procedure. With this module, for each one of the MODIS pixels, nine SEVIRI pixels of the most relative scenes to MODIS pixels regarding date, time, and band were spatially correlated (Figure 3). Additionally, the SEVIRI BT differences (channel 9 BT minus channel 10 BT) correlated to MODIS pixels were calculated and used for the training of the ANN. Therefore, a total of 27 inputs (BT pixel value, distance, and BT difference, for each of the nine selected SEVIRI pixels) were collected for each MODIS pixel. It must be noted that the calculated temperature differences have been successfully used to categorize cloud features according to their optical thickness (Lutz, Inoue, and Schmetz 2003).

The above-mentioned data set was employed to internally validate our approach. Moreover, in order to externally validate the proposed method, one randomly selected MODIS image scene from 15 September 2008 (20:25 UTC) was also selected and used during the external validation procedure (Japkowicz and Shah 2011). The corresponding SEVIRI image was registered at 20:15 UTC (following the HRIT data temporal resolution). This specific date was selected in order to check the robustness and accuracy of the proposed methodology to downscale the SEVIRI TIR imagery to dates from different seasons compared with those from which the original data sample was gathered.

2.3. *Artificial neural networks*

ANNs have gained a great deal of popularity due to their intrinsic capability to establish complex non-linear relationships between data, provided that the training sample is representative of the underlying (unknown) distributions. ANNs enable researchers to approximately reconstruct any non-linear continuous function, and therefore, such a model is very general and flexible (Haykin 2008).

Among the various types of ANNs, the most popular is the multilayer perceptron (MLP). An MLP consists of an input layer, one or more interior layers, and an output layer. Each layer consists of a number of processing elements, also termed units, nodes, or neurons, due to a loose resemblance with biological neural networks. The interior layers are called 'hidden layers' because they are not directly observable from the system inputs and outputs. The most widely used MLP architecture consists of one hidden layer such as that depicted in Figure 4. The reason for the popularity of this architecture is because it has been proved that any continuous function mapping of an n-dimensional input to an m-dimensional output can be implemented exactly by a network with one hidden layer (Hecth-Nielsen 1987).

Each neuron calculates an output $f(\boldsymbol{w}^{\mathrm{T}}\boldsymbol{x})$ where $\boldsymbol{x}$ is the vector of input activations from the preceding layer, $\boldsymbol{w}$ is a vector of weights (sometimes termed synaptic weights), and f is a bounded non-decreasing non-linear function such as the logistic function or the hyperbolic tangent (Reed and Marks 1999). Learning is usually performed through an iterative process during which ANNs modify their weights to store the acquired knowledge about the problem provided in the form of input–output pairs. A schematic representation of the learning process is depicted in Figure 5. The training algorithm for MLP ANNs is usually the back propagation (BP) algorithm or another recent and sometimes computationally more efficient variant (Haykin 2008).

In this work, we employed the scaled conjugate gradient method (Møller 1993; Bishop 1995; Du and Swamy 2006) because of its improved speed compared both to the classical BP algorithm and conventional conjugate algorithms. For a more thorough presentation in

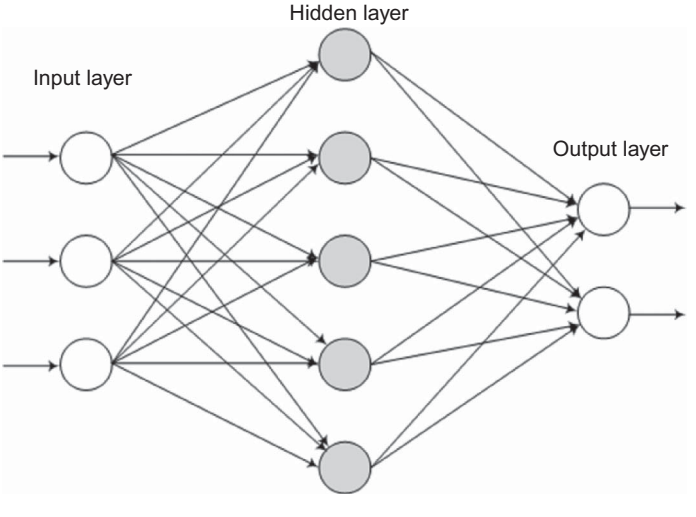

Figure 4. An MLP with one hidden layer.

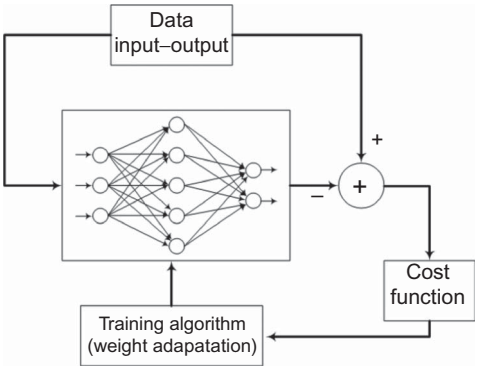

Figure 5. Training of an ANN. The output of the ANN is subtracted from the desired output and this serves as input to the training algorithm that changes the weights of the ANN.

terms of the origin and development of the ANN paradigm, the interested reader can refer to any of the excellent textbooks available (Haykin 2008; Reed and Marks 1999).

Therefore, having a set of ground truth data, an ANN can be used to learn the mapping between inputs and the outputs. Thus, an ANN model does not require explicit knowledge of the input–output mapping. On the other hand, the user should provide the architecture of the MLP. By the term architecture, we imply determination of the number of processing units of the hidden layer (assuming that we adopt the use of only one hidden layer) and sometimes the determination of the input layer, since the output layer is dictated by the nature of the problem. The determination of the 'optimum' architecture requires specific and intense experimentation in order to find the optimum settings. Too simple a model (small number of processing units) will be unable to capture the underlying non-linear relationships (under-fitting), whereas too complex a model could lead to overfitting if no precautions are taken during the training procedure. The most common approach to model selection is the use of grid search, trying varying configurations in a cross-validation procedure (Haykin 2008).

In the case of regression applications, the output neurons are not equipped with a non-linear function f, and the non-linear processing is performed only by the hidden units. For almost all applications, preprocessing of the inputs is required. The simplest example involves normalization of the inputs while in the case of correlated inputs a stage of principal component analysis (PCA) is recommended (Bishop 1995). Since the inputs are indeed correlated in the case of pixel values, a PCA stage was involved and the next section provides a brief overview of this widely used method (Georgoulas, Stylios, and Groumpos 2006; Haykin 2008; Bishop 1995). Figure 6 depicts the overall proposed methodology, where all stages of the methodology are briefly described.

2.4. Dimensionality reduction using PCA

PCA or the Karhunen–Loeve transformation is one of the most popular methods for linear dimensionality reduction (Haykin 2008). PCA linearly transforms the original space (Haykin 2008) by projecting the d-dimensional data onto the l ($l \leq d$) eigenvectors of their covariance matrix corresponding to the l larger eigenvalues. Even if the entire set of the eigenvectors has to be retained, this may also lead to improved performance due to the uncorrelated nature of the new set of features.

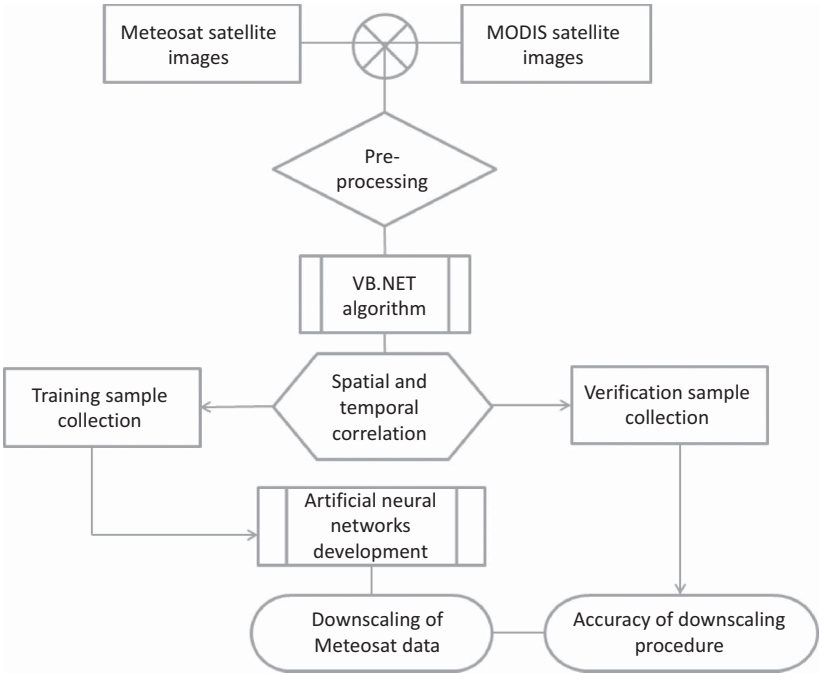

Figure 6. Flow chart of the procedures followed during the downscaling of SEVIRI image scenes.

In practice, for a data set stored in an $n \times d$ matrix (each row corresponds to a data sample and each column corresponds to an input), the algorithm proceeds as follows.

(1) Compute the mean value for each feature and then subtract this mean.
(2) Calculate the covariance matrix of the zero-mean data matrix, its eigenvalues, and its corresponding eigenvectors.
(3) Retain the eigenvectors corresponding to the l largest eigenvalues and project the input vectors onto them to get a reduced representation.

Figure 7 depicts the scatter plot of the values of adjacent pixels (correlation coefficient value = 0.99). Such a high correlation justifies the use of PCA.

2.5. Linear regression

For comparison reasons, a linear regression model was also tested. A linear regression model linearly combines the inputs, also termed regressors. Due to its linear nature, it can effectively be trained using the least squares algorithm. On the other hand, the linear nature of the method makes it suboptimal when the underlying process is non-linear. The output, y, of the model is given by Equation (1):

$$y = c_0 + \mathbf{c}^{\mathrm{T}}\boldsymbol{x} = [\, c_0 \quad \mathbf{c}^{\mathrm{T}} \,] \begin{bmatrix} 1 \\ \boldsymbol{x} \end{bmatrix}, \tag{1}$$

where $\boldsymbol{x}$ is the input vector and c_0 and $\mathbf{c}$ are the regression coefficients.

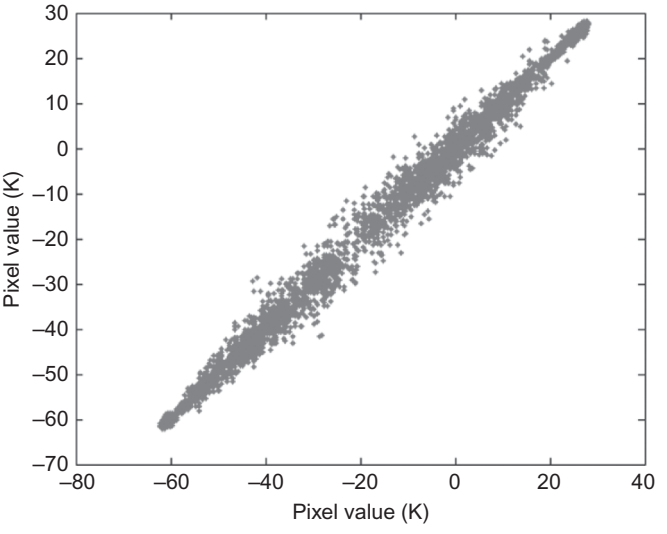

Figure 7. Scatter plot of adjacent pixels from the original low-resolution image.

3. Results

In order to test the proposed integrated approach and compare it to the linear regression model, we applied both internal and external validation approaches (Japkowicz and Shah 2011). For the internal validation procedure, the data collected from the first two sets of images were split into different sets following the procedure of Section 2.2. Then, such data sets were divided into a training set and a test set. This represents the internal validation since both training and testing sets came from the same underlying distribution. The external validation procedure involved a separate set of image samples corresponding to different data, and therefore, they formed a truly independent sample.

Both the MLP and the linear model were trained to 'predict' the value of a finer-scaled pixel based on information collected at a coarser level. As mentioned in Section 2.2, the original information gathered at the coarser level included the nine values of the closest coarse pixels along with their distances from the finer-level pixel, as well as the nine differences corresponding to temperature differences of the two SEVIRI TIR channels used (channel 9 temperature minus channel 10 temperature). Therefore, we used 27 inputs in total. However, as noted in Section 2.4, because of the correlated nature of the input variables, we included a dimensionality reduction stage in order to reduce the original input vector. The number of retained principal components that determined the dimension of the transformed input vector could be derived based on a number of methods such as the retained variance (also termed cumulative percentage of variance explained), using a screen plot (Martinez, Martinez, and Solka 2011), or it could be determined based on the performance of the developed model. The first approach, which acts as a 'filter' without the explicit use of a learning method/model, is more computationally efficient, but the second, which 'wraps' the selection procedure with the involved learning method/model, can lead to better overall performance (Burrell et al. 2007; Guyon and Elisseeff 2003). In this study, we applied the latter, and simultaneously, we tried to find the 'optimum' number of principal components and the 'optimum' architecture (number of hidden nodes) for the MLP.

More specifically, we applied an 'inner–outer' loop scheme. The outer loop was included to assess the performance of the proposed approach while the inner scheme was applied to tune the procedure, in other words, to select the number of retained principal components and the number of hidden units. We varied the number of principal components from 1 to 27 and the number of hidden units from 5 to 60 in increments of 5 units, and we performed all of the corresponding tests.

For the 'outer' scheme, a random resampling approach was employed (Japkowicz and Shah 2011). Therefore, we divided the data set into training and testing sets (80% for training and 20% for testing); this procedure was repeated 30 times, each time randomly reshuffling the original data. Each time the training set was again divided into training, validation, and testing sets (60% for training, 20% for validation, and 20% for testing), and that procedure (the inner loop) was also repeated 10 times using a similar reshuffle scheme. During the inner loop, the validation set was employed to stop the training procedure once there were signs of overfitting. The best configuration (number of principal components and number of hidden units), in terms of mean squared error (MSE) averaged over the 10 trials, was selected and the model was retrained using the original training set (again, 20% was reserved as validation set to avoid overfitting) and the performance was evaluated using the reserved testing set. In this way, we decoupled the parameter selection stage from the estimation of the performance and thus we avoided reaching overly optimistic conclusions about the capabilities of the proposed approach. In the case of the linear regression model, the same training and testing sets were used and the inner loop was employed only for the selection of the best number of principal components.

The procedure revealed that in the case of MLP the 'optimum' number of principal components is 4 (it was consistently selected in all 30 replications of the outer loop), while the number of selected hidden numbers varied between 35 to 50 with a peak at 50, as shown in Figure 8, revealing that further increase in the number of hidden units caused overfitting

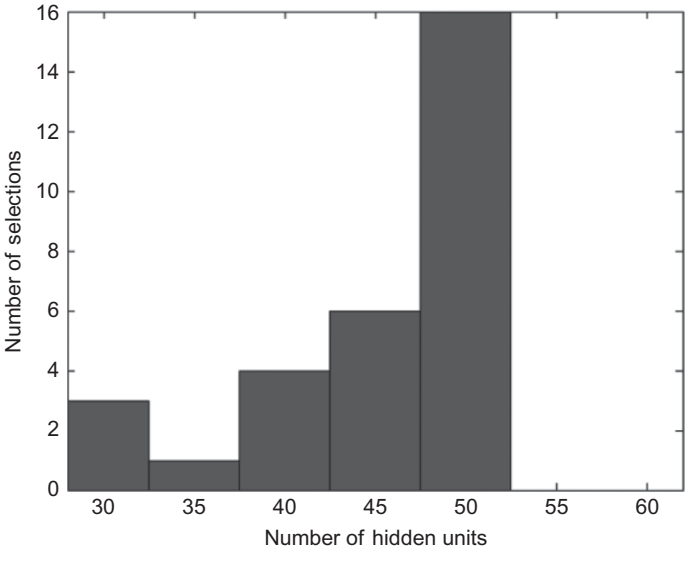

Figure 8. Selected number of hidden units over the 30 replications of the internal validation procedure.

Table 1. Estimated root mean squared error (RMSE) along with respective standard error for the MLP and the linear regression approaches.

Method	Mean RMSE (K)	Standard error (K)
MLP	2.5535	0.0163
Linear	3.1211	0.0063

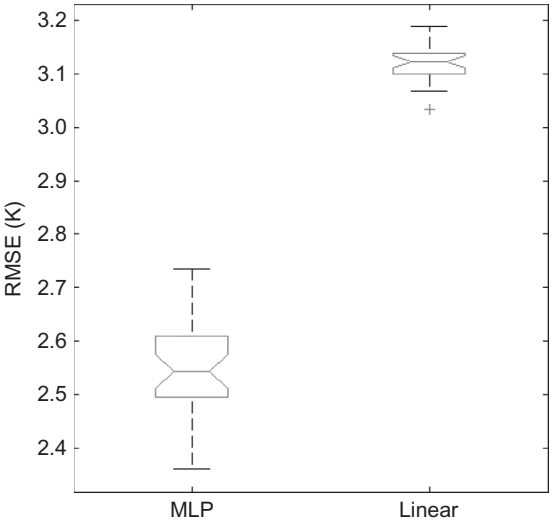

Figure 9. Boxplot depicting the distribution of RMSE for MLP and the linear regression model. Note that MLP compares favourably with the linear model.

effects. In the case of the linear model, the 'optimum number' of principal components was in all but 3 times equal to 27, i.e. the whole set of principal components was retained.

The results in terms of average root mean square error (RMSE) are summarized in Table 1, and a graphical representation is depicted in Figure 9 using boxplots. MLP performed better compared with the linear regression model in terms of RMSE (the Wilcoxon sign-ranked paired test yielded a p-value equal to 1.7344×10^{-6} (Snedecor and Cohran 1980)). The estimated RMSE for internal validation (Table 1) shows a better performance for the MLP approach. The RMSE value of 2.55K is considered acceptable with respect to the wide range of temperatures monitored (−61K to 29K), the different spatial resolution, geometry, and standards of the images used, and the sensors they were derived from.

The above-mentioned internal validation procedure reveals the potential of using an MLP as a method for downscaling. In an attempt to further validate our proposed method, the MLP and the linear regression models were also employed for the 'prediction' of finer-resolution pixels from an image acquired from a subset of 15 September 2008 (20:15 UTC); the SEVIRI image scene was not employed in the aforementioned internal validation procedure. The corresponding MODIS subset (15 September 2008 (20:25 UTC)) was also selected for comparison.

Both the MLP and the linear regression models were trained using all of the pixels that were employed in the internal validation procedure, and the trained models were used to 'predict' the finer-resolution pixels. The results are summarized in Table 2 and Figures 10

Table 2. Estimated root mean squared error (RMSE) and coefficient of determination for the MLP and the linear regression approaches using external data.

Method	RMSE (K)	Coefficient of determination
MLP	2.0995	0.8130
Linear	2.9399	0.6333

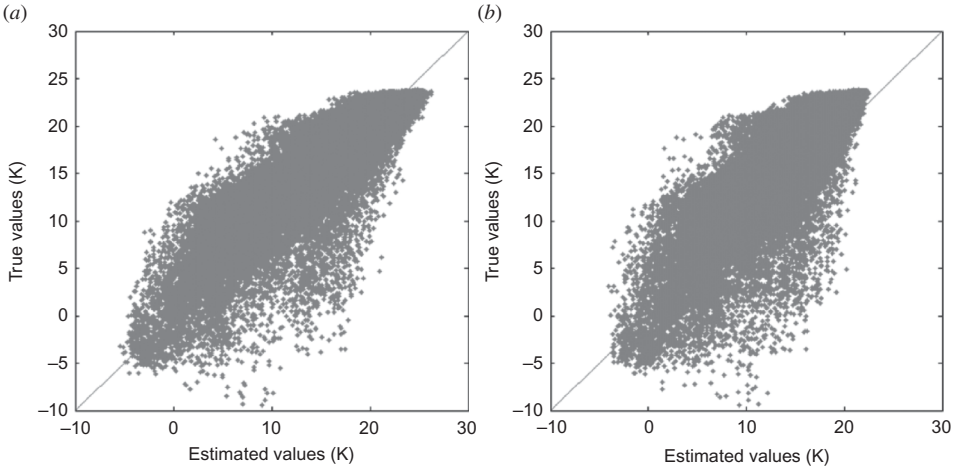

Figure 10. Scatter plot of true *versus* estimated values for (*a*) MLP and (*b*) linear regression models, using external data.

and 11. More analytically in Tables 1 and 2, the RMSE values for the MLP method provide the best results, fluctuating between 2.0K and 2.6K, which is an acceptable estimation of BTs taking into account the wide range of values (Figure 10).

Figures 10(*a*) and (*b*) depict the scatter plots of the model estimates and the true values for the MLP and the linear regression model, respectively. As can be seen from Figure 10, the linear model appears to underestimate the values of the finer-resolution pixels. The MLP model achieves a fairly high coefficient of determination, but some of its estimates are inaccurate.

Figure 11 depicts the visualized outcome of the downscaling process using MLP and the linear regression model for the image acquired on 15 September 2008 (20:15 UTC). As depicted in Figure 11(*d*), the MLP model yields an outcome with more contrast (more high-frequency components), while the linear regression model produces a more blurred version with some circular artefacts that are less pronounced in the MLP. The produced image using MLP model estimations (Figure 11(*c*)) is the more realistic in respect to SEVIRI data (Figure 11(*a*)) and even more so for the MODIS data (Figure 11(*b*)). The cloud formations in Figure 11(*c*) are depicted more clearly than the original image scene (Figure 11(*a*)) but they are smooth and blurry compared with Figure 11(*b*). The smoothing of Figure 11(*c*) is possibly due to the use of nine SEVIRI pixel values for estimating finer-resolution pixel values (Figure 3) without considering the abrupt changes at the edges of every recorded feature and area. Consequently, it is observed that visual improvement (better features detection) for the SEVIRI image was achieved with respect to the initial coarser resolution. In the improved image (Figure 11(*c*)), different cloud types cannot be

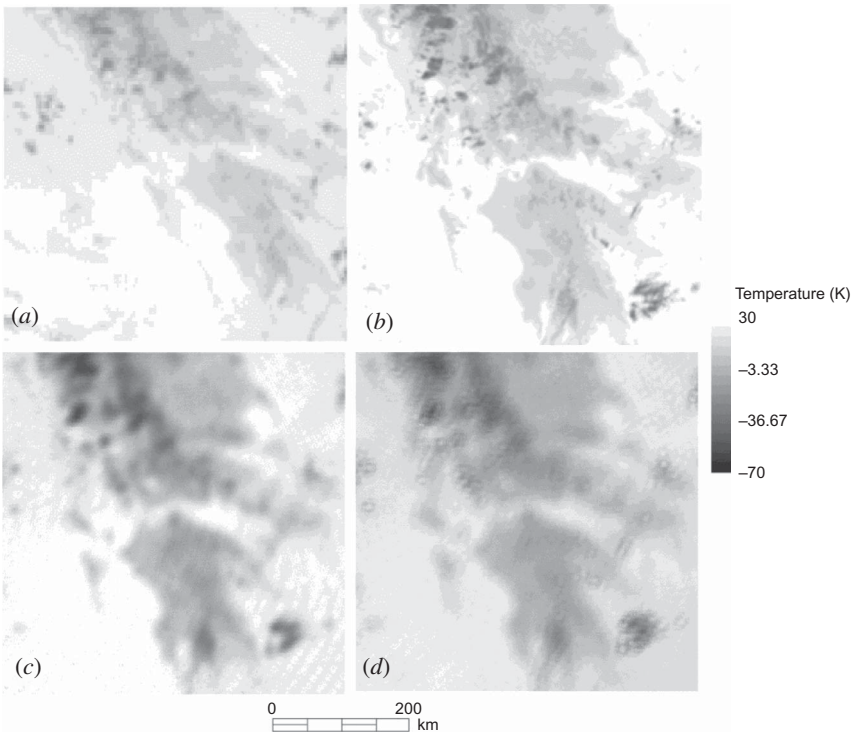

Figure 11. (*a*) Channel 9 of the SEVIRI image; (*b*) channel 31 of the MODIS image; (*c*) downscaled image produced by the MLP model; (*d*) downscaled image produced by the linear regression model (15 September 2008; 20:25 UTC; the depicted area is Greece).

seen as clearly as in the corresponding MODIS image (Figure 11(*b*)), but cloud areas with dense and opaque cloud formations (like cumulonimbus) can be detected (when they exist), contrary to the initial resolution of SEVIRI images where absent. This capability is an important factor for the early detection of convective cloud systems and, in general, the delineation of areas with high convective potential. Contrary to the SEVIRI image produced by the downscaling procedure using MLP (Figure 11(*c*)), the relative image produced using the linear regression model is not satisfactory, having circular aberrations that are not realistic as can be seen from Figures 11(*a*) and (*b*), which show the initial SEVIRI and MODIS images, respectively.

4. Conclusions

In this study, a non-linear regression approach based on MLP was proposed and successfully applied for downscaling TIR SEVIRI images (spectral region, 9.8–11.8 μm). These images are mainly used for operational purposes, providing contiguous data flows during both day and night, and a satisfactory downscaling of these images improved the accuracy of extracted parameters, consequently further increasing their usefulness.

The proposed approach was compared and tested against a linear regression model. The results proved that the non-linear regression scheme for downscaling satellite data (RMSE 2.1–2.6 K; Tables 1 and 2) outperforms the linear regression approach (mean RMSE,

2.9–3.1 K; Tables 1 and 2). The mean RMSE error in the downscaling procedure for the BTs using the MLP approach is considered satisfactory, given the fact that fourfold finer spatial resolution of SEVIRI images was achieved where the training and validation data sets were selected comparing images from two significantly different imageries (SEVIRI and MODIS) according to their scanning modes.

The visual result shows improvement in distinguishing features like opaque cloud formations in the middle and high troposphere relative to the initial SEVIRI image, but there is evident smoothing in the downscaled images.

In future work, we intend also to test local approximators such as piecewise linear models and radial basis function neural networks, since both models employed in this study aim to approximate the underlying function at a global level (Haykin 1999) and to apply ensemble paradigms that have emerged lately as a very promising scheme in predictive modelling (Austin et al. 2012; Wu, Liu, and Jin 2010; Rokach 2010). In future work, we will also examine non-linear dimensionality reduction methods (Van Der Maaten, Postma, and Van Der Herik 2009), since PCA assumes only linear correlations between the inputs which, in some cases, might oversimplify the resulting model. Moreover, we are planning to test edge enhancement techniques and examine how the actual spatial coordinates affect the mapping from the coarse image to one with finer resolution. We also intend to investigate whether the terrene and parallax phenomenon (evident in high clouds at latitudes of Meteosat imagery) imposes specific constraints, dictating the use of spatially dependent models.

Acknowledgements

The authors would like to express special thanks to the anonymous reviewers for their constructive comments that helped to improve the completeness and clarity of the article.

References

Austin, P. C., D. S. Lee, E. W. Steyrberg, and J. V. Tu. 2012. "Regression Trees for Predicting Mortality in Patients with Cardiovascular Disease: What Improvement Is Achieved by Using Ensemble-Based Methods?" *Biometrical Journal* 55: 657–673.

Bishop, C. 1995. *Neural Networks for Pattern Recognition*. Oxford: Clarendon Press.

Burrell, L. S., O. L. Smart, G. Georgoulas, and G. J. Vachtsevanos. 2007. "Evaluation of Feature Selection Techniques for Analysis of Functional MRI and EEG." In *International Conference on Data Mining* (DMIN'07), Las Vegas, NV, June 25–28.

Chu, J. T., J. Xia, C.-Y. Xu, and V. P. Sigh. 2010. "Statistical Downscaling of Daily Mean Temperature, Pan Evaporation and Precipitation for Climate Change Scenarios in Haihe River, China." *Theoretical and Applied Climatology* 99: 149–161.

Deneke, M. H., and A. R. Roebeling. 2010. "Downscaling of METEOSAT SEVIRI 0.6 and 0.8 mm Channel Radiances Utilizing the High-Resolution Visible Channel." *Atmospheric Chemistry and Physics* 10: 9761–9772.

Dibike, B. Y., and P. Coulibaly. 2006. "Temporal Neural Networks for Downscaling Climate Variability and Extremes." *Neural Networks* 19: 135–144.

Du, K. L., and M. N. S. Swamy. 2006. *Neural Networks in a Softcomputing Framework*, 207–215. London: Springer.

Georgiev, C. G., and G. Kozinarova. 2009. "Usefulness of Satellite Water Vapour Imagery in Forecasting Strong Convection: A Flash-Flood Case Study." *Atmospheric Research* 93: 295–303.

Georgoulas, G., C. D. Stylios, and P. P. Groumpos. 2006. "Predicting the Risk of Metabolic Acidosis for Newborns Based on Fetal Heart Rate Signal Classification Using Support Vector Machines." *IEEE Transactions on Biomedical Engineering* 53: 875–884.

Guyon, I., and A. Elisseeff. 2003. "An Introduction to Variable and Feature Selection." *Journal of Machine Learning Research* 3: 1157–1182.

Haykin, S. 1999. "Neural Networks: A Guided Tour." In *Soft Computing and Intelligent Systems: Theory and Applications*, edited by M. M. Gupta and N. K. Sinha, 71–80. San Diego, CA: Academic Press.

Haykin, S. 2008. *Neural Networks and Learning Machines*. 3rd ed. New York: Prentice Hall.

Hecht-Nielsen, R. 1987. "Kolmogorov's Mapping Neural Network Existence Theorem." In *Proceedings of the First IEEE International Joint Conference on Neural Networks,* San Diego, CA, 11–14. New York: IEEE.

Hessami, M., P. Gachon, M. J. T. Ouarda, and A. St-Hilaire. 2008. "Automated Regression-Based Statistical Tool." *Modeling and Software* 23: 813–834.

Japkowicz, N., and M. Shah. 2011. *Evaluating Learning Algorithms; A Classification Perspective*. New York: Cambridge University Press.

Kioutsioukis, I., D. Melas, and P. Zanis. 2008. "Statistical Downscaling of Daily Precipitation over Greece." *International Journal of Climatology* 28: 679–691.

Kolios, S. 2009. "Development of Automated System for the Very Short Range Forecast of Mesoscale Convective Systems Using Meteosat Satellite Imagery." PhD thesis, University of the Aegean, Department of Geography, Greece.

Kolios, S., and H. Feidas. 2012. "An Automated Nowcasting System of Mesoscale Convective Systems for the Mediterranean Basin Using Meteosat Imagery. Part I: System Description." *Meteorological Applications*. doi:10.1002/met.1282.

Liu, D., and R. Pu. 2008. "Downscaling Thermal Infrared Radiance for Subpixel Land Surface Temperature Retrieval." *Sensors* 8: 2695–2706.

Lutz, H.-J., and J. Schmetz. 2003. "Comparison of a Split-Window and a Multi-Spectral Cloud Classification for MODIS Observations." *Journal of Meteorological Society of Japan* 81: 623–631.

Martinez, W. L., A. R. Martinez, and J. Solka. 2011. *Exploratory Data Analysis with Matlab*. London: Chapman and Hall/CRC Press.

Møller, M. F. 1993. "A Scaled Conjugate Gradient Algorithm for Fast Supervised Learning." *Neural Networks* 6: 525–533.

Morel, C., and S. Senesi. 2002. "A Climatology of Mesoscale Convective Systems over Europe Using Satellite Infrared Imagery. I: Methodology." *Quarterly Journal of Royal Meteorological Society* 128: 1953–1971.

Reed, R. D., and R. J. Marks. 1999. *Neural Smithing: Supervised Learning in Feedforward Artificial Neural Networks*. Cambridge, MA: The MIT Press.

Rokach, L. 2010. "Ensembled-Based Classifiers." *Artificial Intelligence Review* 33: 1–39.

Sandholt, I., C. Nielsen, and S. Stisen. 2009. "A Simple Downscaling Algorithm for Remotely Sensed Land Surface Temperature." *American Geophysical Union*. Spring Meeting.

Schmetz, J., P. Pili, S. Tjemkes, D. Just, J. Kerkmann, S. Rota, and A. Rattier. 2002. "An Introduction to Meteosat Second Generation (MSG)." *Bulletin of American Meteorogical Society* 83: 977–992.

Setvak, M., T. D. Linsey, P. Novak, R. M. Rabin, K. P. Wang, J. Kerkmann, M. Radova, and J. Stastka. 2008. "Cold-Ring shaped storm in Central Europe." In *EUMETSAT Meteorological Satellite Conference*. Darmstadt, September 8–12.

Snedecor, G. W., and W. G. Cochran. 1980. *Statistical Methods*. 7th ed. Ames: Iowa State University Press.

Stathopoulou, M., and C. Cartalis. 2009. "Downscaling AVHRR Land Surface Temperatures for Improved Surface Urban Heat Island Estimation." *Remote Sensing of Environment* 113: 2592–2605.

Stein, A., W. G. M. Bastiaanssen, S. De Bruin, A. P. Cracknell, P. J. Curran, A. G. Fabbri, B. G. H. Gorte, J. W. Van Groenigen, F. D. Van Der Meer, and A. Saldana. 1998. "Integrating Spatial Statistics and Remote Sensing." *International Journal of Remote Sensing* 19: 1793–1814.

Stisen, S., I. Sandholt, A. Norgaard, R. Fensholt, and L. Eklundh. 2007. "Estimation of Diurnal Air Temperature Using MSG SEVIRI Data in West Africa." *Remote Sensing of Environment* 110: 262–274.

Sun, D., and R. T. Pinker. 2007. "Retrieval of Surface Temperature from MSG-SEVIRI Observations. Part I. Methodology." *International Journal of Remote Sensing* 28 (23): 5255–5272.

Van Der Maaten, L. P. P., E. O. Postma, and H. J. Van Der Herik. 2009. "Dimensionality Reduction: A Comparative Review." *Journal of Machine Learning Research* 10: 1–41.

Van Der Meer, F. 2012. "Remote-Sensing Image Analysis and Geostatistics." *International Journal of Remote Sensing* 33: 5644–5676.

Vila, A. D., A. L. Machado, H. Laurent, and I. Velasco. 2008. "Forecast and Tracking the Evolution of Cloud Clusters (FORTRACC) Using Satellite Infrared Imagery: Methodology and Verification." *Weather and Forecasting* 23: 233–245.

Wilby, R. L. 1998. "Statistical Downscaling of Daily Precipitation Using Daily Airflow and Seasonal Teleconnection Indices." *Climate Research* 10: 163–178.

Wilby, R. L., S. P. E. Zorita, B. Timbal, P. Whetton, and L. O. Mearns. 2004. "Guidelines for Use of Climate Scenarios Developed From Statistical Downscaling Methods." *Data Distribution Centre of the Intergovernmental Panel on Climate Change*.

Wu, J., M. Liu, and L. Jin. 2010. "Least Square Support Vector Machine Ensemble for Daily Rainfall Forecasting Based on Linear and Nonlinear Regression." *Advances in Neural Network Research and Applications* 67: 55–64.

Zakšek, K., and K. Oštir. 2012. "Downscaling Land Surface Temperature for Urban Heat Island Diurnal Cycle Analysis." *Remote Sensing of Environment* 117: 114–124.

Zakšek, K., and M. Schroedter-Homescheidt. 2009. "Parameterization of Air Temperature in High Temporal and Spatial Resolution from a Combination of the SEVIRI and MODIS Instruments." *ISPRS Journal of Photogrammetry* 64: 414–421.

Zhang, X., H. Jjang, G. Zhou, Z. Xiao, and Z. Zhang. 2012. "Geostatistical Interpolation of Missing Data and Downscaling of Spatial Resolution for Remotely Sensed Atmospheric Methane Column Concentrations." *International Journal of Remote Sensing* 33: 120–134.

Zutita-Milla, R., G. Kaiser, J. G. P. W. Clevers, W. Schneider, and M. E. Schaepman. 2009. "Downscaling Time Series of MERIS Full Resolution Data to Monitor Vegetation Seasonal Dynamics." *Remote Sensing of Environment* 113: 1874–1885.